GEOPHYSICS, VOL. 75, NO. 4 (JULY-AUGUST 2010); P. S151–S161, 14 FIGS.
10.1190/1.3460296

Moveout analysis of wave-equation extended images

Tongning Yang[1] and Paul Sava[1]

ABSTRACT

Conventional velocity analysis applied to images produced by wave-equation migration with a crosscorrelation imaging condition uses moveout information from space lags or focusing information from time lag. However, more robust velocity-estimation methods can be designed to simultaneously take advantage of the semblance and focusing information provided by migrated images. Such a velocity estimation requires characterization of the moveout surfaces defined jointly for space- and time-lags extended images. The analytic solutions to the moveout surfaces can be derived by solving the system of equations representing the shifted source and receiver wavefields. The superposition of the surfaces from many experiments (shots) is equivalent to the envelope for the family of the individual surface. The envelope forms a shape that can be characterized as a cone in the extended space of depth, space lag, and time lag. When imaged with the correct velocity, the apex of the cone is located at the correct reflection depth and at zero space and time lags. When imaged with the incorrect velocity, the apex of the cone shifts in the depth direction and along the time-lag axis. The characteristics of the cones are directly related to the quality of the velocity model. Thus, their analysis provides a rich source of information for velocity model-building. Synthetic examples verify the derived formulas characterizing the moveout surfaces. The analytic formulas match the numeric experiments well, demonstrating the accuracy of the formulas. Based on information provided by the extended imaging condition, future application for velocity updates can benefit from the robustness of the depth-focusing analysis and of the high resolution of the semblance analysis.

INTRODUCTION

A key challenge for imaging in complex geology is accurate construction of the velocity model in the area under investigation. Migration velocity analysis (MVA) is a velocity-model-building technique based on the principle that image-accuracy indicators are optimized when data are imaged correctly. A common procedure for MVA is to examine the alignment of images created with data from many complementary experiments. If images constructed by illuminating a point from various directions are flat, then the velocity model used for imaging is said to be accurate. This idea is usually referred to as the *semblance principle* (Yilmaz, 2001), and it represents the foundation of most velocity-analysis methods used today.

Often, semblance analysis is performed in the angle domain. Angle-domain gathers are an optimal choice for image analysis in complex areas because they are free of complicated artifacts present in surface-offset gathers (Stolk and Symes, 2004). Several methods have been proposed for angle decomposition (Sava and Fomel, 2003; Yoon and Marfurt, 2006; Higginbotham and Brown, 2009). Most of these procedures require decomposition of extrapolated wavefields or of migrated images in components related to the reflection angle. The angle-decomposition procedure based on migrated images requires applying an extended imaging condition (Sava and Fomel, 2006) that implements a point-by-point comparison of the source and receiver wavefields extrapolated from the surface. In general, the comparison is done using simple image-processing procedures such as crosscorrelation applied at every location in the subsurface. If the source and receiver wavefields match each other kinematically, then their crosscorrelation maximizes at zero lag in space and time; otherwise, their crosscorrelation does not maximize at zero lag, indicating a wavefield reconstruction error that may have different causes, e.g., velocity-model inaccuracy.

The source and receiver wavefields used for imaging are 4D objects, functions of spatial coordinates and time (or frequency). For simplicity, we discuss only imaging conditions in the time domain, although our analysis applies equally well to imaging conditions in the frequency domain. For such 4D objects, the images obtained by extended imaging conditions are characterized in general by a 3D space-lag vector and a 1D time-lag scalar. The images constructed

Manuscript received by the Editor 19 May 2009; revised manuscript received 10 February 2010; published online 10 September 2010.
[1]Colorado School of Mines, Center for Wave Phenomena, Golden, Colorado, U.S.A. E-mail: tyang@mines.edu; psava@mines.edu.

with space and time lags can be decomposed into functions of reflection angles using geometric relations between incident and reflected rays (Rickett and Sava, 2002).

Conventional MVA separately exploits space-lag information by semblance analysis (Sava and Biondi, 2004a, 2004b; Shen et al., 2005; Schleicher, 2008; Xia et al., 2008) or time-lag information by depth-focusing analysis (Faye and Jeannot, 1986; MacKay and Abma, 1992, 1993; Nemeth, 1995, 1996; Higginbotham and Brown, 2008). Semblance analysis is based on the space-lag gathers or, more specifically, the horizontal space-lag gathers. It may suffer from the fact that the gathers become less sensitive to steeply dipping reflectors. Thus, the quality of the common-image gather (CIG) is degraded, as discussed by Biondi and Shan (2002) and Biondi and Symes (2004). A similar problem exists for the depth-focusing analysis based on the time-lag gathers. However, the depth-focusing analysis is generally superior in robustness to semblance analysis in processing real data, especially land data, even though its resolution is lower, as indicated by the analysis of Sava and Fomel (2006).

If we consider velocity estimation as an inverse problem, we suggest that a more robust velocity-analysis approach can be designed by optimizing migrated images with all available information provided by the space and time lags. In this way, we can have more constraints on the inversion and simultaneously leverage the robustness of depth-focusing analysis and the high resolution of semblance analysis.

In this paper, we analyze the moveout function for CIGs constructed by extended imaging conditions applied after conventional wavefield extrapolation. We first derive the analytic expression of the moveout function for extended images under the homogeneous media assumption. Next, we focus on the CIGs in multishot experiments and quantitatively analyze their kinematic characteristics, especially the features related to velocity-model error. Finally, we use different synthetic examples to verify the derived analytic moveout functions and to illustrate the application of the analysis in complex geologic models.

WAVE-EQUATION IMAGING CONDITIONS

Under the single-scattering assumption, the seismic migration procedure consists of two main steps: wavefield reconstruction and imaging condition. Wavefield reconstruction involves constructing solutions to a wave equation with recorded seismic data as initial and boundary conditions. Various numeric solutions for the acoustic wave equation can be chosen, depending on the requirements of cost and accuracy. However, regardless of the specific implementation, the reconstruction of the source and receiver wavefields is similar. In a known background velocity model, we forward and backward propagate in time to obtain the source and receiver wavefields from the source wavelet and recorded seismic data, respectively. The reconstructed source and receiver wavefields can be defined as 4D functions of spatial location $\mathbf{x} = (x,y,z)$ and time t:

$$u_S = u_S(\mathbf{x},t), \tag{1}$$

$$u_R = u_R(\mathbf{x},t), \tag{2}$$

where u_S and u_R stand for the source and receiver acoustic wavefields, respectively.

An imaging condition is designed to extract the locations where reflections occur in the subsurface from these reconstructed wavefields. The image $r(\mathbf{x})$ is obtained by exploiting the space and time coincidence of the reconstructed source and receiver wavefields at every subsurface location. A conventional imaging condition (Claerbout, 1985) forms an image as the crosscorrelation of the source and receiver wavefields evaluated at zero lag:

$$r(\mathbf{x}) = \sum_t u_R(\mathbf{x},t)u_S(\mathbf{x},t). \tag{3}$$

An alternative extended imaging condition (Rickett and Sava, 2002; Sava and Fomel, 2006) generalizes the conventional imaging condition by preserving the information from nonzero crosscorrelation lags in the output image:

$$r(\mathbf{x},\boldsymbol{\lambda},\tau) = \sum_t u_S(\mathbf{x}-\boldsymbol{\lambda},t-\tau)u_R(\mathbf{x}+\boldsymbol{\lambda},t+\tau). \tag{4}$$

In equation 4, the quantities $\boldsymbol{\lambda}$ and τ represent the spatial and temporal crosscorrelation lags between the source and receiver wavefields. As in the conventional imaging condition, the extended imaging condition also exploits the space and time coincidence of the wavefields, but it preserves in the output the information corresponding to nonzero space and time lags. As a result of the existence of the lags, the output images are hypercubes, characterized by different lags at each subsurface location $\mathbf{x}$. We refer to these hypercubes as wave-equation extended images. They can help us analyze the accuracy of reconstructed wavefields.

If the local crosscorrelation between the source and receiver wavefields is maximized at zero lag for all four dimensions, those wavefields are extrapolated correctly. If this is not true, we can conclude that the wavefield reconstruction is incorrect, indicating possibilities such as incorrect velocity, incorrect wavefield extrapolation, irregular illumination, or the failure of the single scattering assumption from, for example, the presence of multiples. In this paper, we consider that the errors in wavefield reconstruction are caused by the incorrect velocity model only.

MOVEOUT ANALYSIS FOR EXTENDED IMAGES — POINT SOURCE

The characteristics of extended images can be studied by analyzing CIGs. A reflection event analyzed in a CIG is represented by a multivariable function $z = z(\boldsymbol{\lambda},\tau)$. The geometric shape of this function is often referred to as *moveout* by analogy with surface seismic data. Therefore, extended images are characterized by moveout surface in CIGs. Understanding the moveout surface in the case of correct and incorrect velocities is essential for MVA. How the extended images can be used for MVA is discussed in another publication (Yang and Sava, 2009).

Consider the reflection geometry depicted in Figure 1. The unit vector $\mathbf{n} = \{n_x,n_y,n_z\}$ and the distance d identify the position of a reflection plane relative to the seismic source S. The vector $\mathbf{c} = \{c_x,c_y,0\}$ identifies the fixed horizontal position of CIGs relative to the source position. The vector $\mathbf{z} = \{0,0,z\}$ represents the depth of the image constructed by the imaging condition. We consider here the case where the extended imaging condition involves the time lag τ and only the horizontal space lag $\boldsymbol{\lambda} = \{\lambda_x,\lambda_y,0\}$, but the same logic applies to a more general case where the space lag $\boldsymbol{\lambda}$ is 3D.

Under the assumption of homogeneous media, a wavefield characterizing wave propagation from a point source can be represented by a cone in space and time. The source wavefield is represented by a cone with the origin at zero time and at the source location on the sur-

face, as shown in Figure 2a. Likewise, we construct the receiver wavefield as the mirror image of the source wavefield relative to the reflector, indicated by the black line in Figure 2c. Using these descriptions of the seismic wavefields, we can represent the source and receiver wavefields in space and time by the analytic expressions

$$\|\mathbf{c}+\mathbf{z}\| = Vt, \tag{5}$$

$$\|\mathbf{c}+\mathbf{z}-2d\mathbf{n}\| = Vt, \tag{6}$$

where V is the velocity of the medium, t is the propagation time of the wavefield, $d\mathbf{n}$ characterizes the position of the reflector, and $\mathbf{z} = \{0,0,z\}$, with z representing the depth of the image. Equations 5 and 6 describe the traveltime of waves propagating for the distances SC and $S'C$ shown in Figure 1, respectively. Because S' is the mirror image of the real source S relative to the reflector, the wavefields generated from S and S' arrive at the reflection point C at the same time. As a result, t in both equations is the traveltime for source and mirror-image source wavefields.

Furthermore, we consider the imaging condition as a process by which the image is formed where the source and receiver wavefields coincide. A wavefield generated from the mirror-image source is equivalent to the receiver wavefield in the sense that both coincide with the source wavefield at the reflection point. Thus, equation 6 represents the receiver wavefield under our assumptions, although it describes the mirror image of the source wavefield. As discussed, the imaging conditions identify the position of the reflector by exploiting the time and space coincidence of source and receiver wavefields. In other words, an image forms at the spatial positions where the source and receiver wavefields intersect. Mathematically, this condition is equivalent to identifying the positions that solve the system given by equations 5 and 6, i.e., by solving the system for z at coordinates $\mathbf{c} = \{c_x,c_y\}$. Figure 2a, c, and e illustrates the procedure. Figure 2a and c represents the source and receiver wavefields respectively; the cones are symmetric relative to the reflector. The intersections of the cones occur at different times. However, the locations of the intersections are consistent with the position of the reflector because their projection on the x-z-plane perfectly matches the reflector.

Likewise, the extended imaging condition seeks to find the intersections between the source and receiver wavefields. However, the procedure is different because both wavefields are shifted by the space and time lags in the crosscorrelation. The shifted wavefields

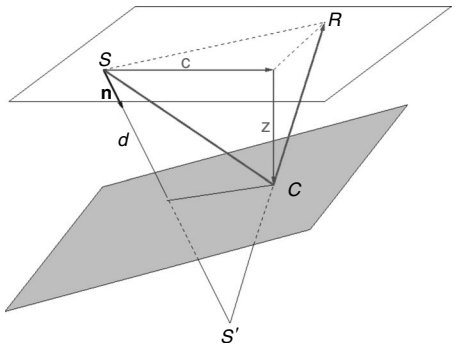

Figure 1. Geometry of a reflection experiment. S, R, and C identify the positions of the source, receiver, and reflection, respectively. The reflector is located at distance d from the source position in the direction of the vector $\mathbf{n}$. The position of the CIG relative to the source is indicated by vectors $\mathbf{c}$ and $\mathbf{z}$.

are functions of the space quantity $\boldsymbol{\lambda} = \{\lambda_x,\lambda_y,0\}$ and time quantity τ. Thus, the extended imaging condition is represented by the system of equations

$$\|\mathbf{c}+\mathbf{z}+\boldsymbol{\lambda}\| = V(t+\tau), \tag{7}$$

$$\|\mathbf{c}+\mathbf{z}-2d\mathbf{n}-\boldsymbol{\lambda}\| = V(t-\tau). \tag{8}$$

The application of the extended imaging condition in equation 4 is equivalent to solving equations 7 and 8. Figure 3 shows an example of the extended imaging condition with horizontal space lag λ_x. The horizontal line represents a planar reflector, and C is the reflection point at the chosen CIG location. The top and bottom arrows represent the propagation of the source and receiver wavefields, and the solid lines denote the approximate wavefronts of the source and receiver wavefields, which intersect at C. Finding this intersection corresponds to applying the conventional imaging condition in equation 3 and solving the system of equations 5 and 6. If we shift the wavefields, the wavefronts move, as denoted by the dashed lines, and intersect at a different depth but the same CIG location. Finding this new intersection corresponds to applying the extended imaging condition in equation 4 and solving the system of equations 7 and 8.

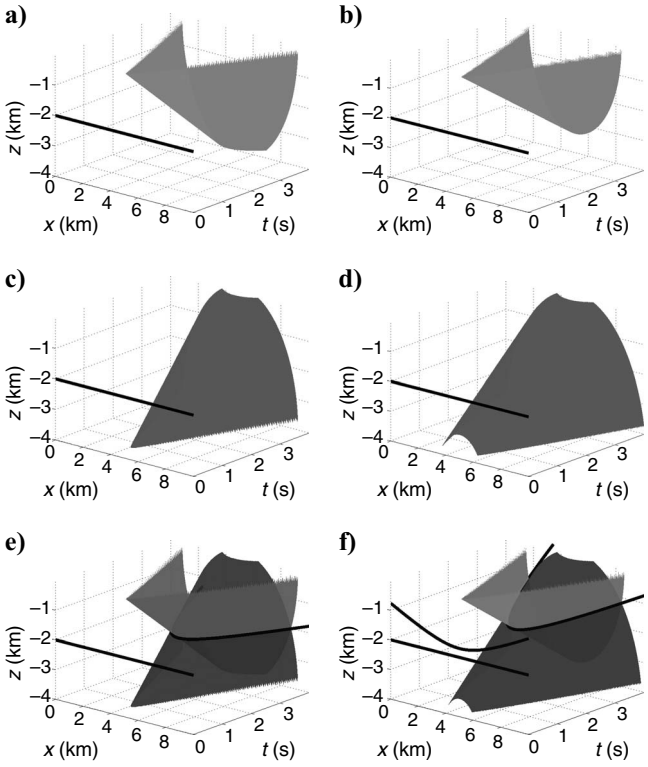

Figure 2. (a) Source wavefield in a constant medium constructed using a correct velocity. (b) Source wavefield in a constant medium constructed using an incorrect velocity. The wavefield has a different shape compared with the wavefield in (a). (c) Receiver wavefield in a constant medium constructed using a correct velocity. (d) Receiver wavefield in a constant medium constructed using an incorrect velocity. The wavefield has a different shape compared with the wavefield in (c). (e) Intersections of the wavefields in (a and c). The projection of the intersection onto the x-z-plane indicates the position of the reflector. (f) Intersections of the wavefields in (b and d). The curved line, which is the projection of the intersection onto the x-z-plane, indicates the position of the reflector. The image is distorted compared with the image in (e).

The solution represents the moveout function $z = z(\boldsymbol{\lambda},\tau)$ at fixed CIG coordinates $\mathbf{c} = \{c_x,c_y,0\}$. This moveout function describes how the depth of the image z changes with the space and time lags.

A formal solution to the system of equations 7 and 8 leads to the following expression:

$$z(\boldsymbol{\lambda},\tau) = (dn_z)K + V\tau\sqrt{K^2 + \frac{\|\mathbf{c}+\boldsymbol{\lambda}\|^2}{(dn_z)^2 - (V\tau)^2}}, \quad (9)$$

where

$$K = 1 - \frac{(\mathbf{c}\cdot\mathbf{n})d - (n_x^2 + n_y^2)d^2 + (\mathbf{c} - d\mathbf{n})\cdot\boldsymbol{\lambda}}{(dn_z)^2 - (V\tau)^2}. \quad (10)$$

Equation 9 represents the moveout function characterizing the shape of the extended images.

To better understand the characteristics of the moveout function, we analyze two special cases of the extended images. The first case corresponds to imaging with space lags only, which is the slice of the moveout surface at $\tau = 0$. Because the square-root term vanishes owing to zero time lag, we obtain a linear moveout function. The coefficient depends on the reflection angles, which justifies the angle-decomposition methods based on slant stacks applied to space-lag CIGs (Sava and Fomel, 2003; Biondi and Symes, 2004; Fomel, 2004). The second case corresponds to imaging with time lag only, which is the slice of the moveout surface at $\boldsymbol{\lambda} = 0$. For this special case, the moveout function is still nonlinear.

As discussed, the goal of our research is to understand the distortions of extended images caused by the velocity-model error. A quantitative analysis of the influence of the velocity error on the extended images is required. When incorrect velocity is used for wavefield reconstruction, the wavefields are extrapolated incorrectly. Applying the imaging condition produces distorted images. Therefore, we must first understand the influence of an incorrect velocity model on the reconstructed wavefields because analytic descriptions of source and receiver wavefields are the key to derive the moveout function. To simplify the problem, we denote the migration velocity $V_m = \rho_V V$, where ρ_V is a constant factor by which the migration velocity differs from the correct velocity.

The source wavefield is reconstructed as in the preceding situation, except that we use an incorrect migration velocity. The wavefield is represented by the cone with radii different from the case of correct velocity. Figure 2b shows the source wavefield reconstructed with incorrect velocity. The wavefield is described by

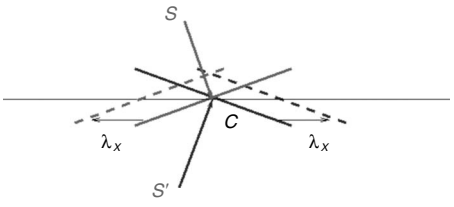

Figure 3. Geometric illustration of the imaging condition. The horizontal line represents a planar reflector. The arrows denoted by S and S' represent the source and receiver rays, respectively. The lines perpendicular to the arrows are the source and receiver wavefronts. They intersect at the reflection point C, which corresponds to the conventional imaging condition. The dashed lines are the wavefront shifted by λ_x; they intersect at the same CIG location but right above the original depth, which corresponds to the extended imaging condition.

$$\|\mathbf{c} + \mathbf{z}\| = V_m t. \quad (11)$$

The situation of the receiver wavefield is more complicated. Unlike the source wavefield, the receiver wavefield is reconstructed by backward propagation of the recorded data. In other words, we reconstruct the cone representing the source wavefield from its origin, but we reconstruct the cone representing the receiver wavefield from its depth slice on the surface. If the correct velocity is used, the cone for the receiver wavefield obtained is the mirror image of the cone for the source wavefield, and both cones are symmetric in space and generated at the same time. In contrast, if an incorrect velocity is used, the cone representing the receiver wavefield has an incorrect radius, as with the source wavefield. Furthermore, the origin of the cone is shifted from its true position in space and time, and the symmetry axis between the two cones deviates from its true spatial location. In summary, the receiver wavefield reconstructed using an incorrect velocity is represented by a cone with incorrect radius, origin, and symmetry axis.

As the receiver wavefield shifts in time, the reconstructed source and receiver wavefields are not triggered at the same moment. It is necessary to introduce a new variable to describe such a deviation in time. Using the concepts of focusing depth d_f and migration depth d_m (MacKay and Abma, 1992), we have $d_f = d/\rho_V$, $d_m = d\rho_V$. We thus define the deviation in time as focusing error t_d, which is quantified by

$$t_d = \frac{d_f - d_m}{V_m} = \frac{d(1-\rho_V^2)}{V\rho_V^2}. \quad (12)$$

The formulas for d_f and d_m are derived under the assumptions of constant velocity, small offset angle, and horizontal reflector; so the formula for focusing error is an approximation when we consider the problem in the real world. If migration velocity V_m is correct, the focusing depth and migration depth are identical and equal to the true depth of the reflection, and the focusing error t_d vanishes. Depending on the ratio between the migrated velocity and true velocity, t_d can be positive or negative.

The receiver wavefield also shifts in space, so symmetry between source and receiver wavefields is maintained but the symmetry plane changes. The plane defined by $d\mathbf{n}$ in the case of correct velocity becomes $d_f\mathbf{n}_m$, where d_f is the focusing depth of the reflection point and $\mathbf{n}_m$ is a new normal vector that is a function of source-receiver location, correct normal $\mathbf{n}$, and the migrated velocity V_m; it can be measured from the migrated image. Given this notation, the receiver wavefield is described by

$$\|\mathbf{c} + \mathbf{z} - 2d_f\mathbf{n}_m\| = V_m(t + 2t_d). \quad (13)$$

Figure 2d shows the receiver wavefield in the case of a horizontal reflector when V_m is smaller than V.

Solving the system of equations 11–13, we obtain the coordinates of the image when the incorrect velocity is used for imaging, as shown in Figure 2f. This solution is equivalent to applying the conventional imaging condition and finding the intersections between the incorrectly reconstructed source and receiver wavefields.

Likewise, we introduce the space and time lags and obtain the expression for the shifted source and receiver wavefields for the case of imaging with incorrect velocity:

$$\|\mathbf{c} + \mathbf{z} + \boldsymbol{\lambda}\| = V_m(t + \tau), \quad (14)$$

$$\|\mathbf{c}+\mathbf{z}-2d_f\mathbf{n}_m-\boldsymbol{\lambda}\| = V_m(t+2t_d-\tau). \quad (15)$$

Solving this system gives the expression for the moveout function of $\boldsymbol{\lambda}$ and τ for incorrect velocity:

$$z(\boldsymbol{\lambda},\tau) = (d_f n_{mz})K + V_m(\tau - t_d)\sqrt{K^2 + \frac{\|\mathbf{c}+\boldsymbol{\lambda}\|^2}{(d_f n_{mz})^2 - V_m^2(\tau - t_d)^2}}, \quad (16)$$

where quantity K is defined by

$$K = 1 - \frac{(\mathbf{c}\cdot\mathbf{n}_m)d_f - (n_{mx}^2 + n_{my}^2)d_f^2 + (\mathbf{c} - d_f\mathbf{n}_m)\cdot\boldsymbol{\lambda}}{(d_f n_{mz})^2 - V_m^2(\tau - t_d)^2}. \quad (17)$$

Comparing the moveout function in equation 16 to the moveout function in equation 9, we observe that the equations share a similar form, although the formula corresponding to the incorrect velocity is more complicated. The complexity arises from the additional term t_d as well as from the fact that d, V, and $\mathbf{n}$ are replaced by d_f, V_m, and $\mathbf{n}_m$. Owing to the existence of t_d, the square-root term is preserved when $\tau = 0$; the space-lag moveout function thus has a nonlinear dependence on the variables.

MOVEOUT ANALYSIS FOR EXTENDED IMAGES — PLANE WAVES

The analytic results discussed in the preceding section have complicated forms and correspond to single-shot experiment, which is not how MVA procedures are implemented in practice. Moreover, the moveout functions are derived based on the assumption of homogeneous media. Therefore, we must reduce the complexity of moveout functions and generalize the analysis to inhomogeneous media.

Figure 4 illustrates a seismic reflection occurring in an inhomogeneous medium. The wave propagation is arbitrary due to the inhomogeneity, as indicated by the curved wavepaths. The corresponding wavefield can also have an arbitrary geometric shape rather than a regular cone; thus, we cannot describe the wavefields using analytic formulas and derive analytic moveout functions. However, they can be approximated as plane waves in the vicinity of the reflection point. Using the same geometry shown in Figure 1, the source and receiver plane waves are described by

$$\mathbf{p}_S\cdot\mathbf{x} = Vt, \quad (18)$$

$$\mathbf{p}_R\cdot(\mathbf{x} - 2d\mathbf{n}) = Vt, \quad (19)$$

where $\mathbf{p}_S$ and $\mathbf{p}_R$ are the unit direction vectors of the source and receiver plane waves, respectively, and $\mathbf{x}$ is the vector sum of $\mathbf{c}$ and $\mathbf{z}$. The value V is defined as the velocity in the locally homogeneous medium around the reflection point and thus is identical for both wavefields.

We can also obtain the shifted source and receiver plane waves by introducing the space and time lags:

$$\mathbf{p}_S\cdot(\mathbf{x}+\boldsymbol{\lambda}) = V(t+\tau), \quad (20)$$

$$\mathbf{p}_R\cdot(\mathbf{x} - 2d\mathbf{n} - \boldsymbol{\lambda}) = V(t-\tau). \quad (21)$$

Solving the system of equations 20 and 21 leads to

$$(\mathbf{p}_S - \mathbf{p}_R)\cdot\mathbf{x} = 2V\tau - (\mathbf{p}_S + \mathbf{p}_R)\cdot\boldsymbol{\lambda} - 2d\mathbf{p}_R\cdot\mathbf{n}, \quad (22)$$

which characterizes the moveout function of space and time lags at a common-image point.

Furthermore, we have the following relations for the reflection geometry:

$$\mathbf{p}_S - \mathbf{p}_R = 2\mathbf{n}\cos\theta, \quad (23)$$

$$\mathbf{p}_S + \mathbf{p}_R = 2\mathbf{q}\sin\theta, \quad (24)$$

where $\mathbf{n}$ and $\mathbf{q}$ are unit vectors normal and parallel to the reflection plane and θ is the reflection angle. Combining equations 22–24, we obtain the moveout function for plane waves:

$$z(\boldsymbol{\lambda},\tau) = d_0 - \frac{\tan\theta(\mathbf{q}\cdot\boldsymbol{\lambda})}{n_z} + \frac{V\tau}{n_z\cos\theta}. \quad (25)$$

The quantity d_0 is defined as

$$d_0 = \frac{d - (\mathbf{c}\cdot\mathbf{n})}{n_z} \quad (26)$$

and represents the depth of the reflection corresponding to the chosen CIG location. This quantity is invariant for different plane waves, assumed constant here.

When incorrect velocity is used for imaging, based on the analysis in the preceding section, we can obtain the moveout function:

$$z(\boldsymbol{\lambda},\tau) = d_{0f} - \frac{\tan\theta_m(\mathbf{q}_m\cdot\boldsymbol{\lambda})}{n_{mz}} + \frac{V_m(\tau - t_d)}{n_{mz}\cos\theta_m}, \quad (27)$$

where d_{0f} is the focusing depth of the corresponding reflection point, V_m is the migration velocity, t_d is the focusing error, and $\mathbf{n}_m$ and $\mathbf{q}_m$ are vectors normal and parallel to the reflection, respectively, which can be measured from the migrated image.

We derive the moveout functions describing extended images for a single seismic experiment. However, typical imaging uses multishot seismic experiments for better illumination of subsurface and imaging redundancy, indicating velocity accuracy. Thus, it is important to understand the characteristics of extended images in such complete seismic-reflection experiments.

The wave equation is a linear partial-differential equation, so its solutions comply with the linear-superposition principle. This is also

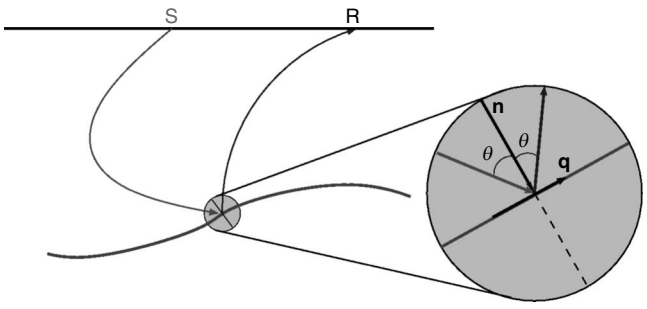

Figure 4. Drawing depicting wave propagation in an inhomogeneous medium. The wavepaths in the local region around the reflection point can be approximated with straight lines.

true for extended images. Thus, the extended images in multishot experiments are a linear superposition of extended images from all single-shot experiments. The extended images from one shot (plane wave) at each subsurface location can be considered as a surface in the extended space z-$\boldsymbol{\lambda}$-τ. The extended images constructed from many shots constitute a family of surfaces. This is a one-parameter family with the reflection angle θ as the parameter because one θ corresponds to one shot (plane wave). By definition, the envelope of a family of surfaces is a surface tangent to each member of the family at some points. Therefore, the extended images in multishot experiments are equivalent to the envelope for the family consisting of the surfaces represented by the extended images from all single-shot experiments.

Based on the formula for the extended images from one plane wave, we can derive the envelope formula by solving the following system of equations:

$$G(\theta,(z,\boldsymbol{\lambda},\tau)) = 0, \tag{28}$$

$$\frac{\partial G}{\partial \theta}(\theta,(z,\boldsymbol{\lambda},\tau)) = 0, \tag{29}$$

where G represents the implicit definition of the moveout function in equation 25 for correct velocity and equation 27 for incorrect velocity. Solving the system yields the following solutions:

$$z(\boldsymbol{\lambda},\tau) = d_0 + \frac{V\tau}{n_z}\sqrt{1-\left(\frac{n_z(\mathbf{q}\cdot\boldsymbol{\lambda})}{V\tau}\right)^2} \tag{30}$$

for correct velocity and

$$z(\boldsymbol{\lambda},\tau) = d_{0f} + \frac{V_m(\tau - t_d)}{n_{mz}}\sqrt{1-\left(\frac{n_{mz}(\mathbf{q}_m\cdot\boldsymbol{\lambda})}{V_m(\tau - t_d)}\right)^2} \tag{31}$$

for incorrect velocity.

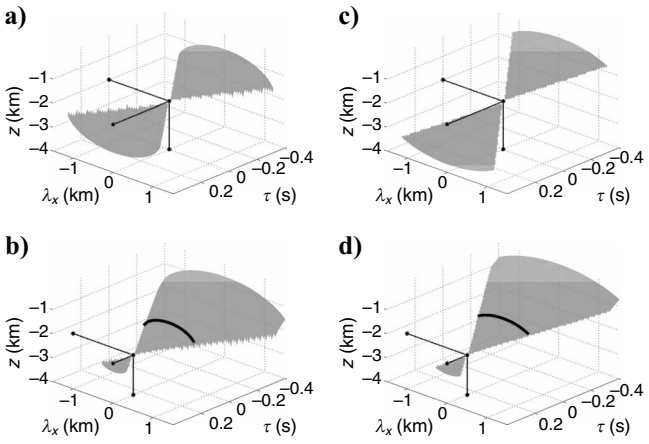

Figure 5. (a and b) Cones formed by the envelope of the moveout surfaces corresponding to individual plane waves for a horizontal reflector. In the correct velocity case (a), the focus of the cone occurs at zero space and time lags. In the incorrect velocity case (b), the focus of the cone shifts to a nonzero time lag. (c and d) Cones formed by the envelope of the moveout surfaces corresponding to individual plane waves for a dipping reflector. In the correct velocity case (c), the focus of the cone occurs at zero space and time lags. In the incorrect velocity case (d), the focus of the cone shifts to a nonzero time lag. The thick line corresponds to the slice of the cone cut at zero time lag.

Analyzing the envelope functions for the cases of correct and incorrect velocities, we note that both envelope functions share a similar form, so they should have similar kinematics. The envelope functions become singular when $\tau = 0$ or $\tau = t_d$ because at these special time lags all individual surfaces corresponding to various experiments intersect at the same location. Mathematically, the envelope function is equivalent to a singular delta function at this τ. Also, the square-root term in both formulas contains a subtraction. We must ensure that the quantity under the square root is nonnegative — otherwise, the formula fails. This failure implies that the range of $\boldsymbol{\lambda}$ is limited, which suggests that we must restrict the range of $\boldsymbol{\lambda}$ when we measure the moveout of reflections.

Given the envelope functions shown in equations 30 and 31, we conclude that the envelope surfaces form cones regardless of the dipping angle and velocity model used for imaging, as shown in Figure 5. However, the shapes of the cones change with velocity and reflector dip. The cones are incomplete because of the limitations of acquisition aperture. When the velocity used for imaging is correct, the apex of the cone is located at zero lags and at the correct depth of the reflection point. In contrast, when the velocity is incorrect, the cone is shifted in depth and in the time-lag direction. The shift in time lag is exactly the focusing error t_d defined before, and the location of the shifted apex is the focusing depth d_{0f}.

If we slice the cone at negative time lags, the slices correspond to the upper half of the cone and thus curve downward. In contrast, the slices correspond to the lower half of the cone and curve upward. The events present in the zero-time-lag slice in the case of incorrect velocity are characterized by the residual moveout used in conventional MVA (Sava and Biondi, 2004a, 2004b; Shen and Symes, 2008), as indicated by the thick line in the Figure 5b and d. Based on the analysis presented here, we can evaluate the accuracy of the velocity model by examining the position of the apex of the cone. If the apex occurs at zero space and time lags, the velocity model is correct. If the apex shifts to nonzero time lags, the migration velocity is incorrect. Thus, the position of the apex of the cone can indicate velocity error.

To summarize, in inhomogeneous media, no analytic moveout function exists to describe exact moveout surfaces for extended images. However, by restricting our analysis to the vicinity of the reflection point and by assuming that the velocity change above the image points is relatively uniform, we can use a plane-wave approximation to derive the analytic functions characterizing extended images. The parameters describing the moveout functions are effective parameters that represent the velocity errors accumulated along wave-propagation paths just as the traveltime errors used in conventional traveltime tomography. These parameters can be transformed into local medium parameters through a tomographic procedure, which we do not discuss here.

EXAMPLES

We illustrate the validity of the moveout functions derived in the preceding sections with several synthetic models. The first model consists of a horizontal reflector embedded in a constant-velocity medium, and the second model consists of a dipping reflector embedded in a constant-velocity medium. We use the first model to verify the accuracy of the moveout function for point sources and plane-wave sources, and we use the second model to verify the accuracy of the envelope functions for plane-wave sources. Extended images are generated for correct and incorrect velocities. The incorrect velocity

is obtained by scaling the correct velocity with a constant factor.

The migrated images corresponding to the horizontal reflector are shown in Figure 6 for correct and incorrect velocities. The reflector is at $z = 1.5$ km, the correct velocity is 2.5 km/s, and the scaling factor is 0.9. The extended images are constructed at CIG location $c_x = 0.5$ km, as indicated by the vertical line. Thus, for a source located at $x = 3$ km, the CIGs analyzed are located at $x = 3.5$ km. To verify the accuracy of the moveout function, we overlay the analytic moveout functions on extended images at fixed time lags or at fixed horizontal space lags.

Figure 7 depicts space-lag extended images corresponding to the chosen CIG location for correct and incorrect velocities. From left to right, the panels correspond to slices at τ of -0.20, 0, and $+0.20$ s. In each column, the upper panels correspond to correct velocities, and the lower panels correspond to incorrect velocities. The dashed lines correspond to the analytic functions in equations 9 and 16, and the solid lines correspond to the analytic functions in equations 25 and 27. In this case, $\mathbf{n}$ and $\mathbf{n}_m$ are the same because the reflector is horizontal. At $\tau = 0$, the moveout event is linear for correct velocity and nonlinear for incorrect velocity, as expected. Comparing the analytic functions derived for point and plane sources, we can observe that the point-source formulas accurately describe the moveout curves in this example. In contrast, the plane-wave formulas are approximations to the point-source formulas, so they are only accurate at small lags and become less accurate for large lags. Finally, we mention that the mismatch at large lag values between the formulas and moveout curves in Figure 7c and f is caused by the diffractions due to truncation of the acquisition array. Such effects are not properly characterized by our formulas, which apply strictly to reflection but not to diffraction.

Figure 8 depicts time-lag extended images for correct and incorrect velocities. From left to right, the panels correspond to λ_x of -0.3, 0, and $+0.3$ km. In each column, the upper and lower panels correspond to correct and incorrect velocities, respectively. The dashed line overlain on each panel corresponds to the analytic functions in equations 9 and 16, and the solid lines correspond to the analytic functions in equations 25 and 27. In both cases, the analytic formulas of the point source accurately describe the moveout surface characterizing extended images. Likewise, the formulas of plane waves are good approximations to the point-source formulas in a small range of lags. This illustrates the accuracy of the analysis of the moveout functions for the extended images.

Figure 9 shows the migrated images of the dipping reflector corresponding to correct and incorrect velocities. The dip of the reflector is about 24°. The correct velocity is 2.5 km/s, and the scaling factor is 0.9. To obtain the images, we use 50 plane-wave sources equally spaced in horizontal slowness and stack the images from all individual experiments. As discussed, the stacked moveout surfaces correspond to the envelope of the surfaces obtained from individual shots. We choose $x = 3.0$ km as the CIG location; the reflection point corresponding to the CIG location is at $z = 1.3$ km.

Figure 10 depicts the moveout surfaces obtained with the correct velocity at different time lags. From left to right, the upper panels display the slices at τ of -0.15, 0, or $+0.15$ s. The lower panels correspond to the same slices but are overlain with the derived analytic envelope function $z(\lambda_x, \tau)$ given by equation 30 for various τ. The correct velocity is used for imaging, so the apex of the cone should be located at zero space and time lags. As expected, a well-focused image is observed in the panel at $\tau = 0, \lambda_x = 0$.

Figure 11 depicts envelopes of moveout surfaces obtained with the incorrect velocity for different time lags. From left to right, the

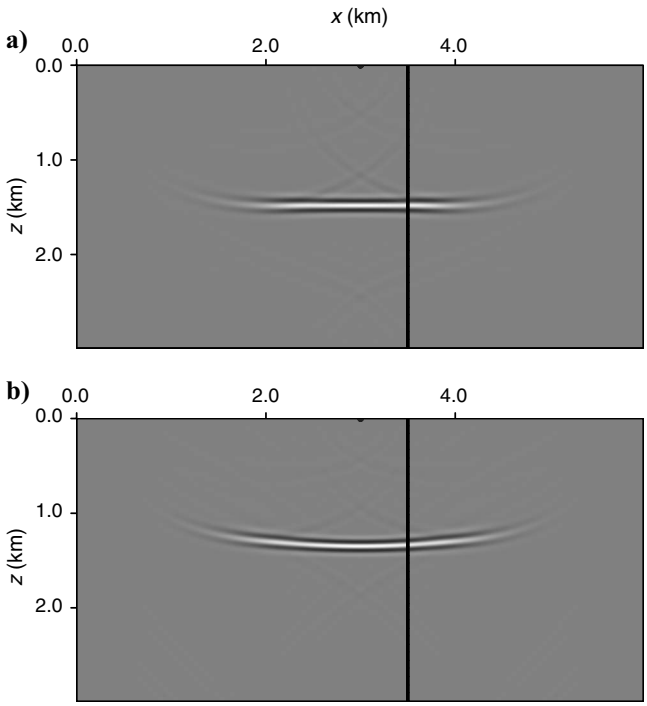

Figure 6. Migrated images corresponding to (a) correct velocity and (b) incorrect velocity. The vertical line indicates the CIG location.

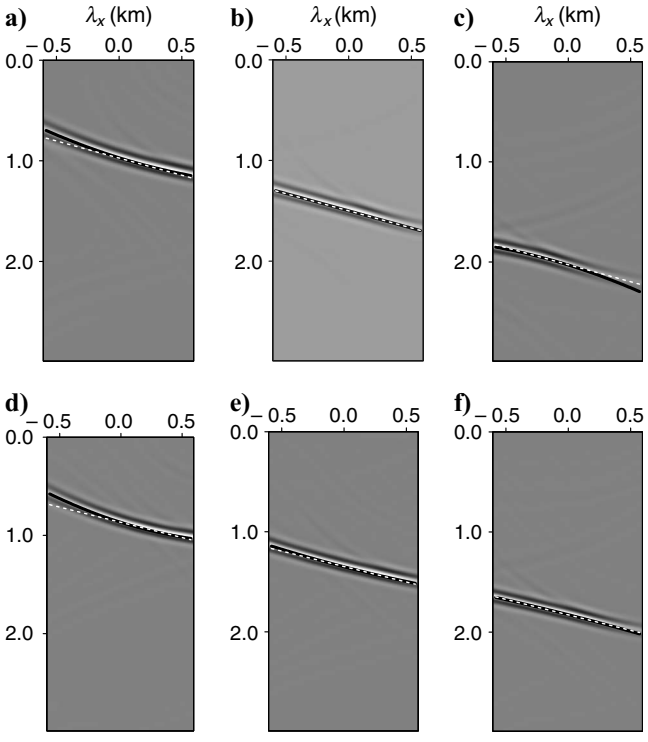

Figure 7. Space-lag CIG chosen at $x = 3.5$ km for τ of -0.20, 0, and $+0.20$ s. Panels (a-c) correspond to correct velocity. Panels (d-f) correspond to incorrect velocity. The solid and dashed lines correspond to the derived analytic functions of point source and plane-wave source, respectively.

upper panels display the slices of the cone at τ of -0.15, 0, or $+0.15$ s. The lower panels correspond to the same slices but are overlain with the derived analytic envelope function $z(\lambda_x,\tau)$ given by equation 31 for various τ. In this case, the dip of the reflector is changed when the image is obtained with an incorrect velocity. Because $\mathbf{n}_m$ is a normal vector to the reflection we obtain, it can be measured on the migrated image. The same logic applies to $\mathbf{q}_m$. The incorrect velocity is used, so the cone shifts such that the apex is not located at $\tau = 0$. As expected, the slice at $\tau = 0$ shows a curved event rather than a focused point, which demonstrates the shift of the apex of the cone. The slice at $\tau = 0.15$ s shows an event curved in a direction opposite to that in Figure 11b, which means the slice is passing the apex of the cone. For correct and incorrect velocities, the analytic functions match the experiments well, demonstrating the accuracy of the envelope functions.

Finally, we use the Sigsbee model (Paffenholz et al., 2002) to illustrate the application of our analysis to inhomogeneous media. Figure 12a shows the velocity profile of the model. The sources are distributed over the left area of the model; thus, they mainly illuminate the left side of the image. Figure 12b and c shows the image migrated with correct and incorrect velocities, respectively.

Figure 13 depicts the moveout surfaces at different time lags for the case of imaging with correct velocity. The panels correspond to slices of the cone at different time lags. Figure 13a shows the slice at $\tau = -0.15$ s. The events in the panel curve downward because the slice is cut at negative τ and corresponds to the upper half of the cone. Figure 13b shows the slice at $\tau = 0$ s, which is cut at the origin of the cone. The events in the panel are focused at zero time lag and space lag, indicating correct velocity. This is consistent with the analysis for the kinematics of extended images in preceding sections.

Figure 14 depicts moveout surfaces for different time lags for the case of imaging with incorrect velocity. The panels correspond to

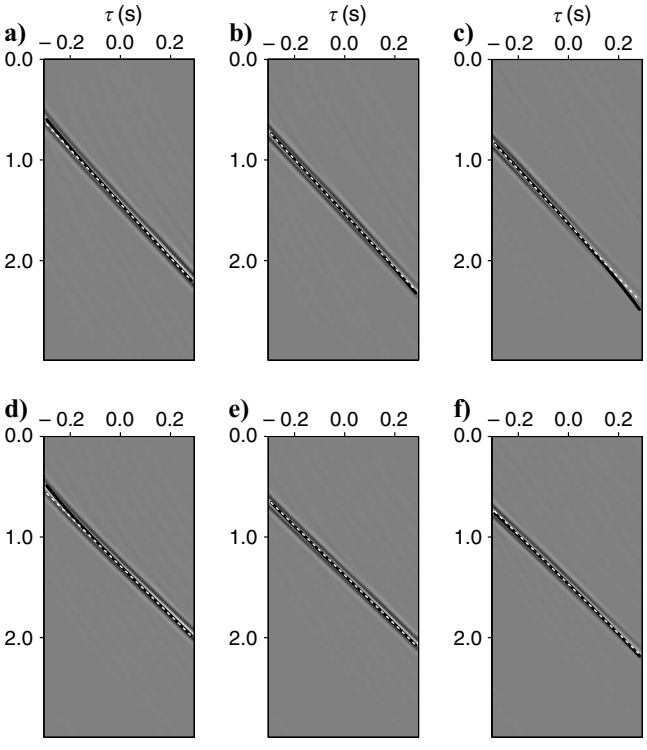

Figure 8. Time-lag CIG chosen at $x = 3.5$ km for λ_x of -0.3, 0, and $+0.3$ km. Panels (a-c) correspond to correct velocity. Panels (d-f) correspond to incorrect velocity. The solid and dashed lines correspond to the derived analytic functions of point source and plane-wave source, respectively.

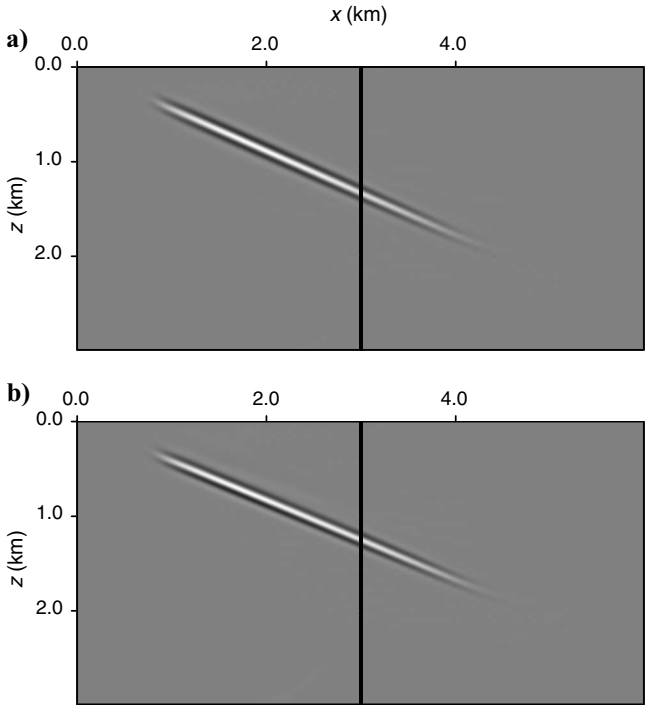

Figure 9. Migrated images corresponding to (a) correct velocity and (b) incorrect velocity. The vertical line indicates the CIG location.

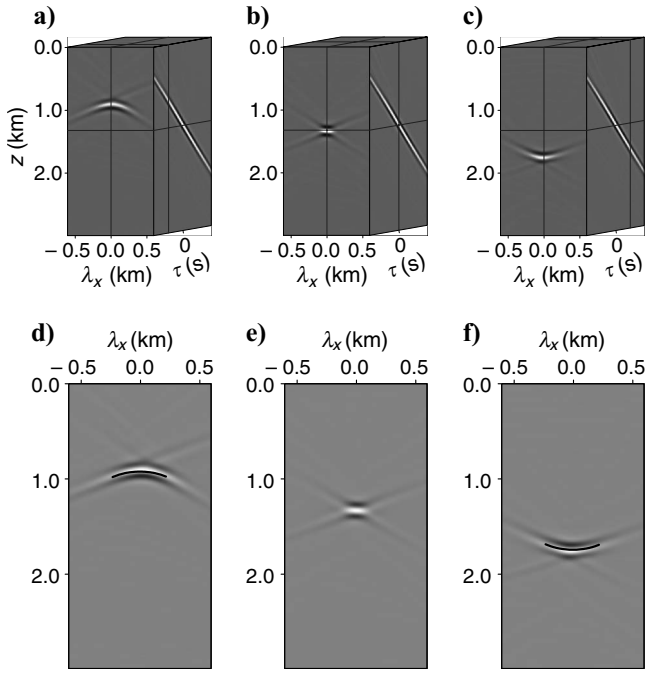

Figure 10. Envelope of the moveout surfaces at different time lags for correct velocity. (a-c) Slices at τ of -0.15, 0, and $+0.15$ s, respectively. (d-f) The same slices overlain by the derived analytic envelope function.

slices of the cone at different time lags. Because a higher migration velocity is used, the origin of the cone is expected to shift to negative τ. Figure 14a shows the slice at $\tau = -0.15$ s. The shallow events in the panel focus at zero space lag, which means the slice is cut at the origin of the cone for these events. Deeper events have the focus of the cone at other values of τ. Figure 14b shows the slices at $\tau = 0$ s. The events in the panels curve upward because the slice is cut away from the focus of the cone.

DISCUSSION

Extended imaging conditions have been used as sources of information for MVA. For example, Biondi and Sava (1999), Shen et al. (2003), Sava and Biondi (2004b), Shen et al. (2005), and Shen and Symes (2008) use space-lag extensions for MVA, whereas Higginbotham and Brown (2008), Brown et al. (2008), and Yang and Sava (2009) use time-lag extensions for MVA. Among the interesting questions one can ask, based on the analysis presented in this paper, are "What is the connection between the two sets of extensions?" and "Is the information provided by space and time lags redundant or complementary?" As indicated, the space- and time-lags extensions are not independent of one another. By observing reflectors in space-lag gathers (at $\tau = 0$) or in time-lags gathers (at $\boldsymbol{\lambda} = 0$), we are exploring subsets of the same object, as seen in Figure 6. Therefore, the z-$\boldsymbol{\lambda}$-τ gathers capture more completely the behavior of events in the extended space and provide access to more complete information to be used for velocity update. It is easier to evaluate the behavior of the cones characterizing a reflection event by observing them in their entirety rather than by observing subsets.

On the other hand, using space- and time-extended gathers, we can better formulate the optimization process that could be used for velocity model updating. For example, conventional wavefield-based MVA that relies on differential semblance optimization (Shen et al., 2005; Symes, 2008) indicates velocity can be optimized by minimizing the objective function of space lags gathers at $\tau = 0$:

$$\min \frac{1}{2}\|r(z,\lambda_x,\lambda_y)\sqrt{\lambda_x^2+\lambda_y^2}\|^2, \tag{32}$$

where λ_x and λ_y are the horizontal components of the $\boldsymbol{\lambda}$ and $r(z,\lambda_x,\lambda_y)$ represents an extended image gather. This objective function corre-

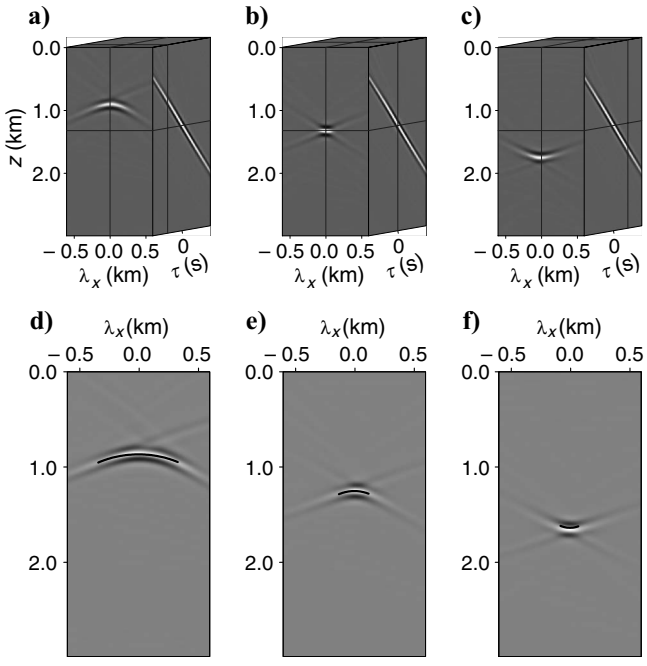

Figure 11. Envelope of the moveout surfaces at different time lag for incorrect velocity. (a-c) Slices at τ of -0.15, 0, and $+0.15$ s, respectively. (d-f) The same slices overlain by the derived analytic envelope function.

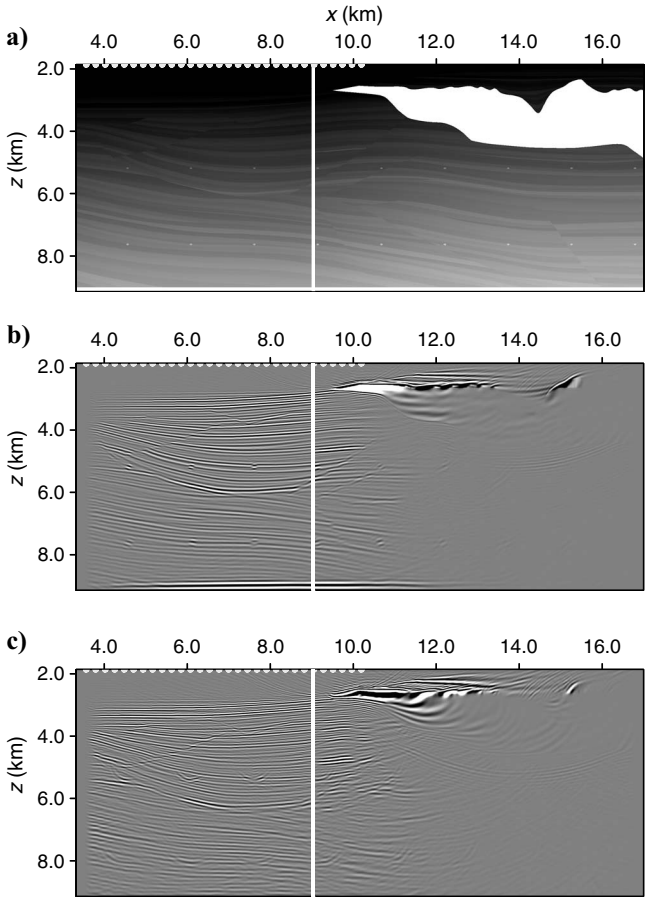

Figure 12. (a) Velocity profile of the Sigsbee model. The migrated images correspond to (b) correct velocity and (c) incorrect velocity. The vertical line indicates the CIG location.

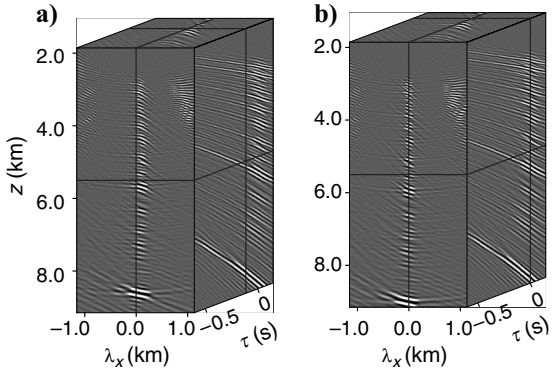

Figure 13. Moveout surfaces at different time lags for correct velocity. Slices of the cube at (a) τ of -0.15 s and (b) τ of 0 s.

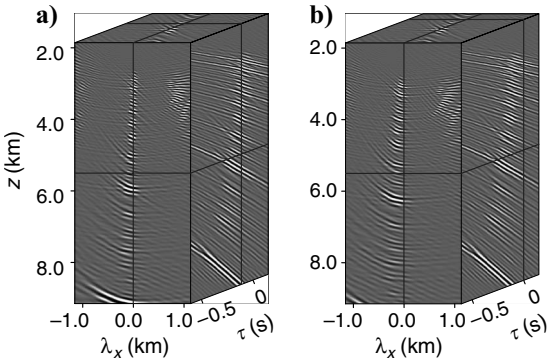

Figure 14. Moveout surfaces at different time lags for incorrect velocity. Slices of the cube at (a) τ of -0.15 s and (b) τ of 0 s.

sponds to the case when we penalize reflector energy outside zero space lag but not the reflector energy at zero space lag. From the analysis presented in this paper, it is apparent that this type of objective function is partial. We really need to penalize all defocused events at all lags (including zero space lag) by the same amount, dependent on how far the apex of the respective event departs from zero time lag. An objective function formulated this way includes the information at zero time lag (the semblance information) as well as the information at zero space lag (the focusing information), thus being more robust and effective for MVA. This topic is discussed in Yang and Sava (2009), and we do not elaborate further on it in this paper.

Finally, an important consideration for practical application of this methodology is computing cost. Computing extended images as a function of both space and time lags is costlier than computing extended images as a function of space lag or time lag separately. On the other hand, there is more information in extended images mixing space and time lags. Therefore, we need to balance the cost and benefits of the extended images. For example, we can reduce the cost by not evaluating the extended images at regions that are inappropriate for velocity update, such as salt bodies. Also, the extended images might be evaluated at relatively sparse locations in the image along the inline and crossline directions to further reduce the cost. However, this may decrease the spatial resolution of the velocity update, so a trade-off between cost and resolution must be made. Furthermore, it is possible to restrict the range of space and time lags to the extent necessary to capture the characteristic of the reflection events.

CONCLUSIONS

An extended imaging condition offers the possibility to design robust MVA methods that simultaneously exploit conventional semblance analysis and depth-focusing analysis. The analytic moveout functions provide quantitative descriptions of the shapes of events in extended images. The envelope of the moveout function characterizing extended images constructed from multiple experiments forms cones in the lags-depth domain. The apex of the cone represents a well-focused image of the reflector. If velocity is correct, the apex appears at zero space and time lags and correct depth; otherwise, the apex shifts to nonzero time lags and an incorrect depth. Such a characteristic can indicate velocity error for tomographic techniques. Synthetic examples verify the validity of the analytic moveout functions and demonstrate that the analysis for properties of the extended images holds even for complex media.

ACKNOWLEDGMENTS

This work is supported in part by the sponsors of the Center for Wave Phenomena at Colorado School of Mines and by a research grant from Statoil. The authors thank the editor and associate editor Yike Liu of *Geophysics* for important suggestions and Yu Zhang and other anonymous referees for careful critiques, which greatly improved the manuscript.

REFERENCES

Biondi, B., and P. Sava, 1999, Wave-equation migration velocity analysis: 69th Annual International Meeting, SEG, Expanded Abstracts, 1723–1726.

Biondi, B., and G. Shan, 2002, Prestack imaging of overturned reflections by reverse time migration: 72nd Annual International Meeting, SEG, Expanded Abstracts, 1284–1287.

Biondi, B., and W. Symes, 2004, Angle-domain common-image gathers for migration velocity analysis by wavefield-continuation imaging: Geophysics, **69**, 1283–1298.

Brown, M. P., J. H. Higginbotham, and R. G. Clapp, 2008, Velocity model building with wave equation migration velocity focusing analysis: 78th Annual International Meeting, SEG, Expanded Abstracts, 3078–3082.

Claerbout, J. F., 1985, Imaging the earth's interior: Blackwell Scientific Publications, Inc.

Faye, J. P., and J. P. Jeannot, 1986, Prestack migration velocities from focusing depth analysis: 56th Annual International Meeting, SEG, Expanded Abstracts, 438–440.

Fomel, S., 2004, Theory of 3D angle gathers in wave-equation imaging: 74th Annual International Meeting, SEG, Expanded Abstracts, 1053–1056.

Higginbotham, J. H., and M. P. Brown, 2008, Wave equation migration velocity focusing analysis: 78th Annual International Meeting, SEG, Expanded Abstracts, 3083–3086.

———, 2009, Wave-equation simulation and angle-domain imaging for acquisition testing, velocity analysis, and more: 71st Conference & Technical Exhibition, EAGE, Extended Abstracts, U040–U043.

MacKay, S., and R. Abma, 1992, Imaging and velocity estimation with depth-focusing analysis: Geophysics, **57**, 1608–1622.

———, 1993, Depth-focusing analysis using a wavefront-curvature criterion: Geophysics, **58**, 1148–1156.

Nemeth, T., 1995, Velocity estimation using tomographic depth-focusing analysis: 65th Annual International Meeting, SEG, Expanded Abstracts, 465–468.

———, 1996, Relating depth-focusing analysis to migration velocity analysis: 66th Annual International Meeting, SEG, Expanded Abstracts, 463–466.

Paffenholz, J., B. McLain, J. Zaske, and P. Keliher, 2002, Subsalt multiple attenuation and imaging: Observations from the Sigsbee 2b synthetic dataset: 72nd Annual International Meeting, SEG, Expanded Abstracts, 2122–2125.

Rickett, J., and P. Sava, 2002, Offset and angle-domain common image-point gathers for shot-profile migration: Geophysics, **67**, 883–889.

Sava, P., and B. Biondi, 2004a, Wave-equation migration velocity analysis — I: Theory: Geophysical Prospecting, **52**, 593–606.

———, 2004b, Wave-equation migration velocity analysis — II: Subsalt imaging examples: Geophysical Prospecting, **52**, 607–623.

Sava, P., and S. Fomel, 2003, Angle-domain common image gathers by wavefield continuation methods: Geophysics, **68**, 1065–1074.

———, 2006, Time-shift imaging condition in seismic migration: Geophysics, **71**, no. 6, S209–S217.

Schleicher, J., 2008, Residual depth moveout and velocity determination for parametric media: Geophysics, **73**, no. 5, VE361-VE367.

Shen, P., C. Stolk, and W. Symes, 2003, Automatic velocity analysis by differential semblance optimization: 73rd Annual International Meeting, SEG, Expanded Abstracts, 2132–2135.

Shen, P., and W. W. Symes, 2008, Automatic velocity analysis via shot profile migration: Geophysics, **73**, no. 5, VE49–VE59.

Shen, P., W. Symes, S. Morton, and H. Calandra, 2005, Differential semblance velocity analysis via shot profile migration: 74th Annual International Meeting, SEG, Expanded Abstracts, 2249–2253.

Stolk, C. C., and W. W. Symes, 2004, Kinematic artifacts in prestack depth migration: Geophysics, **69**, 562–575.

Symes, W. W., 2008, Migration velocity analysis and waveform inversion:

Geophysical Prospecting, **56**, 765–790.
Xia, X., Y. Ren, and S. Jin, 2008, Tomographic migration-velocity analysis using common angle image gathers: 78th Annual International Meeting, SEG, Expanded Abstracts, 3103–3106.
Yang, T., and P. Sava, 2009, Wave-equation migration velocity analysis using extended images: 79th Annual International Meeting, SEG, Expanded Abstracts, 3715–3718.
Yilmaz, O., 2001, Seismic data analysis, 2nd ed.: SEG.
Yoon, K., and K. J. Marfurt, 2006, Reverse-time migration using the Poynting vector: Exploration Geophysics, **37**, 102–107.